In-plane transport properties of heavily δ-doped GaAs n-i-p-i superlattices: Metal-insulator transition, weak and strong localization

T. Schmidt* and St. G. Müller[†]

Institut für Technische Physik I, Universität Erlangen, Erwin-Rommel-Strasse 1, D-90851 Erlangen, Germany

K. H. Gulden[‡]

Institut für Technische Physik I, Universität Erlangen, Erwin-Rommel-Strasse 1, D-90851 Erlangen, Germany
and Electronics Research Laboratory, University of California, Berkeley, California 94720

C. Metzner[§] and G. H. Döhler

Institut für Technische Physik I, Universität Erlangen, Erwin-Rommel-Strasse 1, D-90851 Erlangen, Germany

(Received 29 July 1996)

We performed intralayer-transport measurements on heavily δ-doped GaAs n-i-p-i superlattices in the temperature range of 4–300 K. The n-layer electron density was varied by applying a bias voltage between the selectively contacted n- and p-type layers. This tunability allowed the observation of the disorder-induced metal-insulator transition in a doping superlattice. We compare the experimental electron-density dependence of the mobility at $T=4$ K with theoretical predictions. Good agreement is achieved in the metallic regime, solving the multisubband Boltzmann equation in relaxation-time approximation and close to the metal-insulator transition, applying a self-consistent current-relaxation theory. Furthermore, we analyze the electron conductivity data of both the metallic and insulating phases as functions of temperature and magnetic field oriented perpendicular to the doping layers. The magnetic field as well as the temperature dependence of the conductivity give evidence for weak localization of the metallic phase. In the strongly localized insulating regime our data show a transition from activated high temperature to weakly temperature-dependent low-temperature behavior. A detailed model is elaborated which explains this observation as transition from thermally activated transport over critical barriers of the disorder potential to phonon-assisted tunneling. [S0163-1829(96)03144-X]

I. INTRODUCTION

Despite intensive study over many years, the metal-insulator transition (MIT) of disordered semiconductors continues to be a major field in solid-state physics. In principle, two alternative methods to induce the MIT can be distinguished if we consider n-type semiconductor material which is sufficiently heavily doped to exhibit metallic transport properties:

Impurity-density- and the *magnetic-field-induced* MIT's result from a reduction of the overlap of the impurity wave functions in an uncompensated semiconductor by reducing the doping density or applying a magnetic field, respectively. The electrons are localized on the impurity states. The characteristic feature of this type of transition is that the electron and donor densities are identical.

The *disorder-* or *electron-density-induced* MIT results from a variation of the random disorder potential and the electron density by introducing compensating impurities. The electrons are localized in the minima of the fluctuating disorder potential. Typical of that type of transition is that the electron density is smaller than the donor density.

Most of the experimental work on the MIT has been performed on *three-dimensional* (3D) bulk-semiconductor material (for a general review see Refs. 1–3). Although considerable progress was reported recently, in particular the understanding of the impurity-density induced MIT remains incomplete and a topic of controversial discussion.[4]

The disorder-induced MIT of Si/SiO$_2$ metal-oxide-semiconductor (MOS) structures was the first extensively investigated MIT in a *quasi-two-dimensional* (quasi-2D) system. Instead of introducing compensating impurities as in 3D bulk material, the electron density in the inversion layer of a single sample was tuned by applying a gate voltage. Early work on the MIT in MOS systems was reviewed in Ref. 5. Later the magnetic-field-induced MIT was studied in the weak doping regime both in modulation-doped GaAs/Al$_x$Ga$_{1-x}$As single- and multiple-quantum-well structures,[6,7] as well as n-type δ-doped GaAs samples.[8] An impurity-density-induced MIT was observed in n-type δ-doped Si structures.[9] Recently, the MIT in the integer and fractional quantum Hall regime in GaAs/Al$_x$Ga$_{1-x}$As heterostructures has attracted considerable interest.[10]

Little attention, however, has been paid to the appealing perspectives of heavily δ-doped semiconductor structures with respect to the disorder-induced MIT. To our knowledge only two studies of this type have been reported.[11,12] In both cases the transport in gated n-type δ-doped GaAs structures was investigated as a function of the electron density.

In the present work we report experimental and theoretical results which demonstrate that δ-doped n-i-p-i superlattices[13] provide an excellent model system to investigate the disorder-induced MIT of a quasi-2D electron gas (as proposed more than a decade ago[14]). One of the major advantages of these structures is the tunability of the carrier
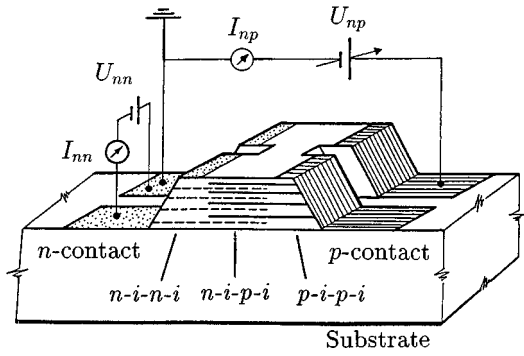
FIG. 1. Schematic diagram of the δ-n-i-p-i mesa with selective contacts and the external electrical circuit.

density and, hence, the number of occupied subbands by an external bias voltage applied through selective contacts.[15] What makes δ-doped n-i-p-i samples different from conventional MOS structures is that they contain not only quasi-2D electron and hole systems but also 2D impurity systems. Furthermore both the random disorder potential and the carrier scattering at low temperature are exclusively due to the ionized impurities. Thus, neither unknown, unspecifiable interface roughness perturbations as in MOS structures nor alloy scattering as in heterostructures influence the in-plane transport in δ-doped n-i-p-i superlattices. Last but not least, the wave functions have a well-defined parity with respect to the impurity positions which imposes specific selection rules for intersubband scattering absent in MOS systems.

The paper is organized as follows. In Sec. II we present the sample design and experimental details. Section III is devoted to a discussion of the electron-density dependence of the low-temperature mobility. Special emphasis is put on the density regime close to the disorder-induced MIT. In Sec. IV we study the influence of low magnetic fields on the conductivity of the quasi-2D electron gas with respect to weak localization. Subsequently a comprehensive analysis of the temperature dependence of the conductivity in both the metallic and insulating regimes is given in Sec. V. We conclude with a brief summary of the results in Sec. VI.

II. SAMPLE AND EXPERIMENT

A. Sample design

The physical properties of a δ-n-i-p-i superlattice are entirely determined by its design parameters *donor concentration* $n_D^{(2)}$, *acceptor concentration* $n_A^{(2)}$, and *interlayer distance* d. The sample for the present investigation was grown by molecular-beam epitaxy using a shadow-mask technique.[15] Selective contacts to the n- and p-type layers of the central n-i-p-i region itself are readily provided via the lateral n-i-n-i and p-i-p-i regions by standard optical lithography (Fig. 1). The application of an improved technique with a thin epitaxially grown shadow mask[16] permitted the fabrication of micrometer-scale devices with typical lateral sample dimensions of 20 μm. The GaAs n-i-p-i superlattice consists of 16 δ-doped p- and 15 δ-doped n-type layers which were grown in an alternating sequence with an interlayer separation of $d=75$ nm. Experimentally determined values of the concentrations of Be acceptors and Si donors

will be given in Sec. II B. The superlattice was grown on a 1-μm-thick undoped $Al_{0.4}Ga_{0.6}As$ buffer layer on a semi-insulating GaAs substrate, and capped by 200 nm of undoped $Al_{0.3}Ga_{0.7}As$ and 30 nm of undoped GaAs.

B. Experimental technique

In order to perform conductance measurements as a function of the electron density (and, hence, of the disorder) we used a setup which allowed to measure the n- and p-layer conductances as a function of the bias U_{np} applied between selective n- and p-type contacts. As a consequence of the indirect real-space energy gap of δ-n-i-p-i superlattices[13] the interlayer electron-hole recombination currents are lower by orders of magnitude than the intralayer currents driven by small voltages U_{nn} or U_{pp} applied between two n- or p-type contacts. Thus the carrier gas in the n- and p-layers can be described by quasi-Fermi levels ϕ_n and ϕ_p. The quasi-Fermi-level difference is determined by

$$\Delta\phi_{np} = \phi_n - \phi_p = eU_{np}. \tag{1}$$

Simultaneously a two-point measurement of the n-layer conductance G_{nn} was performed as a function of the bias U_{np}

$$G_{nn}(U_{np}) = \left.\frac{I_{nn}}{U_{nn}}\right|_{U_{np}}. \tag{2}$$

In order to minimize the influence the voltage drop between the two n contacts on the electron density, the voltage U_{nn} was chosen as small as possible (not higher than 1 mV). Furthermore, the conductance data were averaged with respect to the sign of U_{nn}. The p-layer conductance $G_{pp}(U_{np})$ was measured analogously. A typical example of the measured n-layer conductance is shown in Fig. 2(a) for temperature $T=4$ K.

The electrical room-temperature characterization of the sample allowed the experimental determination of the actual densities of electrically active Si and Be dopants in the n- and p-type δ-layers, respectively. Details are given in Appendix A. The obtained values are $n_A^{(2)}=7.7\times10^{12}$ cm^{-2} and $n_D^{(2)}=6.6\times10^{12}$ cm^{-2}.

Temperature-dependent measurements have been performed in a standard Oxford ^{4}He liquid-flow cryostate with a Hewlett-Packard HP 4141B dc current/voltage source/monitor unit which also recorded the sample temperature by measuring the resistance of a calibrated Si diode. For magnetotransport experiments, we used an Oxford ^{3}He/^{4}He cryostate with a 16.5 T superconducting magnet in connection with a Keithley 220 current source and a Keithley 199 voltmeter.

C. Data preparation

In the present study, we investigate the transport properties as a function of the 2D electron density $n^{(2)}$. From the measured $G_{nn}(U_{np})$ data, we deduced the mobility $\mu_n(n^{(2)})$ and conductivity $\sigma_n(n^{(2)})$ by calculating the relation $n^{(2)}(U_{np})$ with a semiclassical Thomas-Fermi method.[17] In this simplest local-density approximation of the inhomogenous carrier gas the electron-density equation
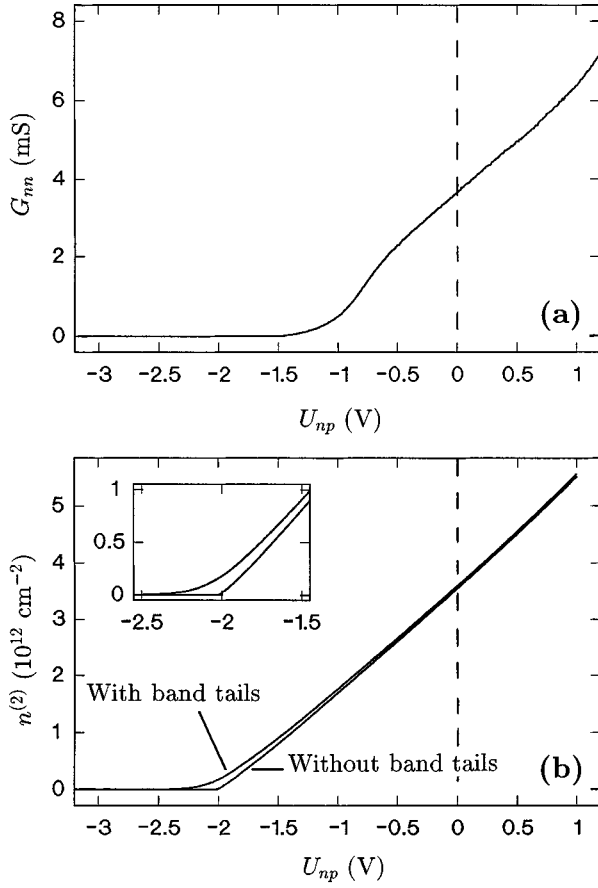
FIG. 2. (a) Measured electron conductivity and (b) calculated electron density, both as a function of the bias voltage for temperature $T=4$ K. The dashed vertical lines mark the ground state corresponding to $U_{np}=0$ V.

$$n^{(3)}(z)=\int_{-\infty}^{\infty}d\epsilon\, D_c^{(3)}(\epsilon,z)f(\epsilon,\phi_n-V_{sc}(z)) \qquad (3)$$

and an analogous hole-density equation for $p^{(3)}(z)$ are solved self-consistently with the Poisson equation within one period of the superlattice

$$\frac{d^2}{dz^2}V_{sc}(z)=\frac{e^2}{\epsilon\epsilon_0}[(n_D^{(2)}\delta(z)-n_A^{(2)}\delta(z-d))$$

$$+(p^{(3)}(z)-n^{(3)}(z))]. \qquad (4)$$

Here z denotes the growth direction,

$$D_c^{(3)}(\epsilon,z)=\frac{1}{2\pi^2}\left(\frac{2m_c}{\hbar^2}\right)^{3/2}\sqrt{\epsilon}\,\Theta(\epsilon-V_{sc}(z)) \qquad (5)$$

the 3D density of states (DOS) for the electrons (subscript c for conduction band), $f(\epsilon,\phi_n-V_{sc}(z))$ the Fermi-Dirac distribution, m_c the effective electron mass and $V_{sc}(z)$ the self-consistent superlattice potential. Integration of $n^{(3)}(z)$ in the z direction over the superlattice period yields the area density $n^{(2)}$.

An improved version of the Thomas-Fermi method which takes band tailing due to the random distribution of the ionized impurities into account is described in Appendix B.
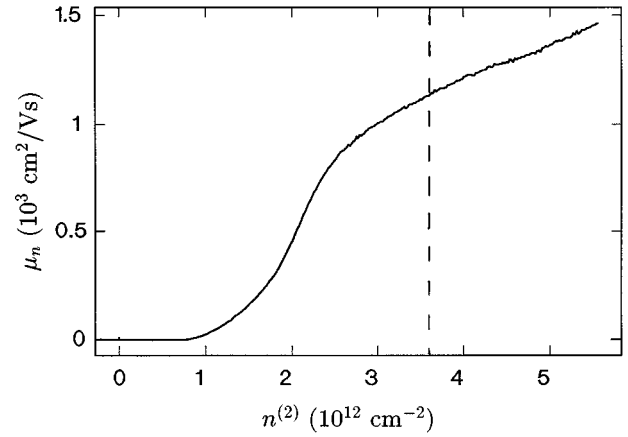
FIG. 3. Electron mobility as a function of the electron density for temperature $T=4$ K. The dashed vertical line marks the ground state corresponding to $U_{np}=0$ V.

The results of both Thomas-Fermi algorithms are depicted in Fig. 2(b). Due to the high doping concentrations the examined p-type sample is a so-called semimetal, i.e., both the electron density $n^{(2)}$ and, according to the macroscopic charge-neutrality condition

$$p^{(2)}-n^{(2)}=n_A^{(2)}-n_D^{(2)}>0, \qquad (6)$$

the hole density $p^{(2)}$ are nonvanishing in the ground state of the superlattice ($U_{np}=0$ V). With increasing negative bias electrons (holes) are extracted from the n layers (p layers) until $n^{(2)}$ vanishes ($p^{(2)}$ assumes its minimum value $n_A^{(2)}-n_D^{(2)}$) at the threshold voltage $U_{np}^{th}\approx-2.0$ V. The sample's p-type character provides the possibility to deplete the n-layer electron gases completely, which is indispensable for an investigation of the MIT of the electron layers. Under forward bias additional electrons (holes) are injected. The injection of free carriers is experimentally limited by the exponentially increasing interlayer leakage current I_{np} which obscures the $G_{nn}(U_{np})$ data. Figure 2(b) shows that the influence of the band tails is restricted to the threshold region.

By calculating $n^{(2)}(U_{np})$ with the improved Thomas-Fermi algorithm, we computed the mobility $\mu_n(n^{(2)})$ and conductivity $\sigma_n(n^{(2)})$ as a function of the electron density from the measured $G_{nn}(U_{np})$ data. The lengthy transformation formulas which require a detailed consideration of contact resistances and sample dimensions are given in Appendix C.

III. DENSITY DEPENDENCE OF THE MOBILITY

The purpose of this section is a detailed comparison of the density dependence of the electron mobility with theoretical predictions for the low-temperature case of $T=4$ K. The measured electron mobility $\mu_n(n^{(2)})$ plotted in Fig. 3 decreases with decreasing electron density. At a density of about $n^{(2)}=1.0\times10^{12}$ cm^{-2} the mobility even vanishes. This behavior will be interpreted below as a disorder-induced MIT due to electron localization in the fluctuating potential of the randomly distributed ionized donors.

A. Self-consistent subband structure

The quantum-mechanical determination of the subband structure of the δ-n-i-p-i superlattice[18] is the starting point for the calculation of the low-temperature mobility. We confine ourselves to the case of $T=0$ K, as the conductivity calculations below will be performed in the $T=0$-K limit as well.

Within the effective-mass approximation we solved the one-dimensional Schrödinger equation for the electrons in the growth direction,

$$\left\{-\frac{\hbar^2}{2m_c}\frac{d^2}{dz^2}+V_{\mathrm{sc}}(z)+V_{x,c}(z)\right\}\varphi_{c,\nu}(z)=\epsilon_{c,\nu}\varphi_{c,\nu}(z),\tag{7}$$

self-consistently with the corresponding Schrödinger equation for the holes and the Poisson equation (4). Above, $\varphi_{c,\nu}(z)$ and $\epsilon_{c,\nu}$ are the electron wave functions and subband-edge energies for subband index ν. The exchange potential $V_{x,c}(z)$ for the electrons was chosen according to Slater[19] as

$$V_{x,c}(z)=-1.477c_0(n^{(3)}(z))^{1/3},\tag{8}$$

with $c_0=e^2/4\pi\epsilon\epsilon_0$. A complete subband wave function with wave vector $\mathbf{k}_\parallel$,

$$\psi_{c,\nu,\mathbf{k}_\parallel}(\mathbf{r})=\frac{1}{\sqrt{S}}e^{i\mathbf{k}_\parallel\mathbf{r}_\parallel}\,\varphi_{c,\nu}(z)\tag{9}$$

is given by a plane wave parallel to the layers multiplied by the wave function in growth direction $\varphi_{c,\nu}(z)$. S is the sample cross section. The corresponding eigenvalues

$$\epsilon_{c,\nu,\mathbf{k}_\parallel}=\frac{\hbar^2\mathbf{k}_\parallel^2}{2m_c}+\epsilon_{c,\nu}\tag{10}$$

are given as the sum of the parabolic dispersion parallel to the layers and the subband-edge energies. The 3D electron density was calculated according to

$$n^{(3)}(z)=\sum_\nu\,|\varphi_{c,\nu}(z)|^2n_\nu^{(2)},\tag{11}$$

with the electron density of the νth subband,

$$n_\nu^{(2)}=\int_{-\infty}^{+\infty}d\epsilon\,D_{c,\nu}^{(2)}(\epsilon)\Theta(\phi_n-\epsilon),\tag{12}$$

and the 2D DOS

$$D_{c,\nu}^{(2)}(\epsilon)=\frac{m_c}{\pi\hbar^2}\Theta(\epsilon-\epsilon_{c,\nu}).\tag{13}$$

The total area density results from

$$n^{(2)}=\sum_\nu\,n_\nu^{(2)}.\tag{14}$$

Analogous expressions were used for the holes.

The dependence of the electron density of the individual subbands on the quasi-Fermi-level difference is depicted in Fig. 4. With growing $\Delta\phi_{np}$ the population of the first subband starts at the threshold value of $\Delta\phi_{np}^{\mathrm{th}}\approx-2.0$ eV. The
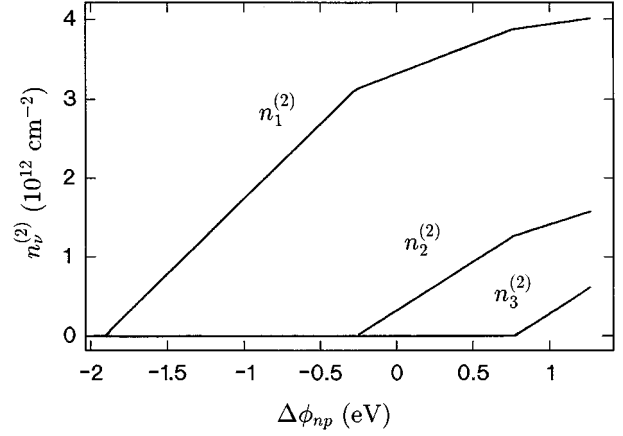
FIG. 4. Electron density of the individual subbands depending on the quasi-Fermi-level difference.

second and third subbands follow at -0.3 and 0.8 eV, respectively. Beyond a forward bias of 1.0 V the experimental determination of the conductance is no longer reliable due to the increasing I_{np} current. Figure 5 shows the resulting superlattice band structure for various excitation levels. The energy spacing between different subband edges exceeds the thermal broadening of the Fermi distribution at $T=4$ K by two orders of magnitude. Therefore the $T=0$-K approximation is well justified for the band-structure calculation. Note that miniband formation due to coupling of subbands of neighboring superlattice-potential wells is irrelevant due to the wide and high barriers of our superlattice.

In principle, the electron density of individual subbands may be determined from measurements of the longitudinal magnetoresistance.[20] Our experimental efforts in this direction failed as the observed Shubnikov–de Haas oscillation periods exhibited, after Fourier transformation to resolve contributions of different occupied subbands, no consistent bias-voltage dependence. We attribute this problem to a mixing of the oscillations of the n-i-p-i region and those of n-i-n-i regions whose electron density is rather bias voltage independent.

B. Boltzmann equation

In order to calculate the electron mobility we solved the multisubband Boltzmann equation in the relaxation-time approximation.[21,22] A comprehensive review is given in Ref. 23. Charge transport parallel to the layers results from the interplay between the accelerating electric field $\mathbf{E}$ and hampering scattering processes which are described by the perturbation operator H_{int}. In the $T=0$-K limit only elastic ionized impurity scattering has to be taken into account. Hence the perturbation operator is explicitly given by

$$H_{\mathrm{int}}=\sum_\alpha\,V^{\mathrm{tot}}(\mathbf{R}_{\parallel,\alpha}),\tag{15}$$

with $V^{\mathrm{tot}}(\mathbf{R}_{\parallel,\alpha})$ being the potential of the ionized donor α at location $\mathbf{R}_{\parallel,\alpha}$.

The coupled multisubband Boltzmann equations which consider both intrasubband and intersubband scattering read

$$-\frac{e}{m_c}\hbar\mathbf{k}_\parallel\cdot\mathbf{E}\frac{\partial f_{c,\nu,\mathbf{k}_\parallel}}{\partial\epsilon_{c,\nu,\mathbf{k}_\parallel}}$$

$$=\sum_{\nu',\mathbf{k}_\parallel'}[\gamma_{c,\nu',\mathbf{k}_\parallel'\to c,\nu,\mathbf{k}_\parallel}\cdot f_{c,\nu',\mathbf{k}_\parallel'}(1-f_{c,\nu,\mathbf{k}_\parallel})$$

$$-\gamma_{c,\nu,\mathbf{k}_\parallel\to c,\nu',\mathbf{k}_\parallel'}\cdot f_{c,\nu,\mathbf{k}_\parallel}(1-f_{c,\nu',\mathbf{k}_\parallel'})]. \quad (16)$$

$f_{c,\nu,\mathbf{k}_\parallel}$ is the value of the Fermi distribution at energy $\epsilon_{c,\nu,\mathbf{k}_\parallel}$, and $|\psi_{c,\nu,\mathbf{k}_\parallel}\rangle$ denotes the corresponding subband state. For the transition probability $\gamma_{c,\nu,\mathbf{k}_\parallel\to c,\nu',\mathbf{k}_\parallel'}$ between $|\psi_{c,\nu,\mathbf{k}_\parallel}\rangle$ and $|\psi_{c,\nu',\mathbf{k}_\parallel'}\rangle$, we obtain, in the first-order Born approximation,

$$\gamma_{c,\nu,\mathbf{k}_\parallel\to c,\nu',\mathbf{k}_\parallel'}$$

$$=\frac{2\pi}{\hbar}|\langle\psi_{c,\nu,\mathbf{k}_\parallel}|H_{\text{int}}|\psi_{c,\nu',\mathbf{k}_\parallel'}\rangle|^2\cdot\delta(\epsilon_{c,\nu,\mathbf{k}_\parallel}-\epsilon_{c,\nu',\mathbf{k}_\parallel'}). \quad (17)$$

Linearization of Eq. (16) with respect to the electric field allows the calculation of the mobilities of the different subbands within a multisubband relaxation-time approximation. The corresponding relaxation times $\tau_{c,\nu}$ of individual subbands are implicitly determined by

$$\phi_n-\epsilon_{c,\mu}=\sum_\nu K_{\mu\nu}\tau_{c,\nu} \quad (18)$$

through inversion of the matrix

$$K_{\mu\nu}=\frac{2\pi^2\hbar^3}{m_c^2 S}\sum_{\mathbf{k}_\parallel,\mathbf{k}_\parallel'}\left[\delta_{\mu\nu}\sum_\lambda\langle|\langle\psi_{c,\mu,\mathbf{k}_\parallel}|H_{\text{int}}|\psi_{c,\lambda,\mathbf{k}_\parallel'}\rangle|^2\rangle_{\text{average}}\cdot\delta(\epsilon_{c,\mu,\mathbf{k}_\parallel}-\phi_n)\delta(\epsilon_{c,\lambda,\mathbf{k}_\parallel'}-\phi_n)\cdot\mathbf{k}_\parallel^2\right.$$

$$\left.-\langle|\langle\psi_{c,\mu,\mathbf{k}_\parallel}|H_{\text{int}}|\psi_{c,\nu,\mathbf{k}_\parallel'}\rangle|^2\rangle_{\text{average}}\cdot\delta(\epsilon_{c,\mu,\mathbf{k}_\parallel}-\phi_n)\delta(\epsilon_{c,\nu,\mathbf{k}_\parallel'}-\phi_n)\cdot\mathbf{k}_\parallel\cdot\mathbf{k}_\parallel'\right]. \quad (19)$$

The effective mobility μ_n is calculated from the different subband mobilities $\mu_{n,\nu}$,

$$\mu_n=\frac{1}{n^{(2)}}\sum_\nu\mu_{n,\nu}n_\nu^{(2)}, \quad \mu_{n,\nu}=\frac{e}{m_c}\tau_{c,\nu}. \quad (20)$$

The remaining task is the computation of the scattering matrix element $\langle|\langle\psi_{c,\nu,\mathbf{k}_\parallel}|H_{\text{int}}|\psi_{c,\nu',\mathbf{k}_\parallel'}\rangle|^2\rangle_{\text{average}}$. Here $\langle\rangle_{\text{average}}$ averages over all possible donor configurations assuming their totally uncorrelated distribution. Screening of the impurity potentials due to free electrons is assumed to be linear which is justified for high electron density.

1. Screening in 3D local-density approximation

The standard linear-screening theory for the screening of an external potential by a homogenous 3D electron gas is the semiclassical Thomas-Fermi theory (see, e.g., Ref. 24) based on the local-density approximation (3D LDA). The screened Coulomb potential has the Yukawa shape

$$V^{\text{tot}}(\mathbf{R}_\parallel)=\frac{c_0}{|\mathbf{r}-\mathbf{R}_\parallel|}\exp\left(-\frac{|\mathbf{r}-\mathbf{R}_\parallel|}{L_n}\right), \quad (21)$$

with the screening length L_n given by

$$L_n^{-2}=\frac{3e^2m_c}{\epsilon\epsilon_0\hbar^2}\left(\frac{1}{3\pi^2}\right)^{2/3}n^{(3)1/3}. \quad (22)$$

In order to apply these formulas to δ-n-i-p-i structures with their z-dependent electron-density we set $n^{(3)}=n^{(3)}(z=0)$ in Eq. (22), i.e., we used the maximum value of $n^{(3)}(z)$. This overestimates the screening as the actual $n^{(3)}(z)$ is nonuniform and decays with increasing distance from the doping layer (Fig. 5). Nevertheless, the approximation is good due to the fact that the characteristic decay length of $n^{(3)}(z)$ exceeds the screening length L_n for typical electron densities. From the computation of the scattering matrix element

$$\langle|\langle\psi_{c,\nu,\mathbf{k}_\parallel}|H_{\text{int}}|\psi_{c,\nu',\mathbf{k}_\parallel'=\mathbf{k}_\parallel+\mathbf{q}_\parallel}\rangle|^2\rangle_{\text{average}}$$

$$=n_D^{(2)}\int d\mathbf{R}_\parallel|\langle\psi_{c,\nu,\mathbf{k}_\parallel}|V^{\text{tot}}(\mathbf{R}_\parallel)|\psi_{c,\nu',\mathbf{k}_\parallel+\mathbf{q}_\parallel}\rangle|^2, \quad (23)$$

it follows that the intrasubband-scattering efficiency decreases with increasing wave vector. This explains why the mobility $\mu_{n,\nu}$ of a given subband in Fig. 6 grows with increasing Fermi wave vector $k_{F,\nu}$ (or electron density $n_\nu^{(2)}$) as long as no intersubband scattering occurs. The effective mobility $\mu_n(n^{(2)})$ shows three different regimes corresponding to the number of occupied subbands:

For $n^{(2)}<3.1\times10^{12}$ cm^{-2} one subband is occupied. Thus only $1\to1$ intrasubband scattering processes occur and $\mu_n(n^{(2)})$ grows monotonously.

For 3.1×10^{12} cm$^{-2}<n^{(2)}<5.1\times10^{12}$ cm^{-2}, two subbands are occupied. $1\to1$ and $2\to2$ intrasubband processes occur whereas $1\to2$ or $2\to1$ intersubband processes are forbidden since the screened Coulomb potential $V^{\text{tot}}(\mathbf{R}_\parallel)$ is even in z [Eq. (21)] and the wave functions $\varphi_{c,1}(z)$ and $\varphi_{c,2}(z)$ have different parity (Fig. 5). Scattering in the second subband is less efficient than in the first one because $n_2(z)$ vanishes at the sites of the donor scattering centers, while $n_1(z)$ attains its maximum (Fig. 5). Nevertheless, the slope of the averaged mobility $\mu_n(n^{(2)})$ drops by almost a factor of 2 when the occupation of the second subband starts as the electron-density growth per subband is roughly halved.
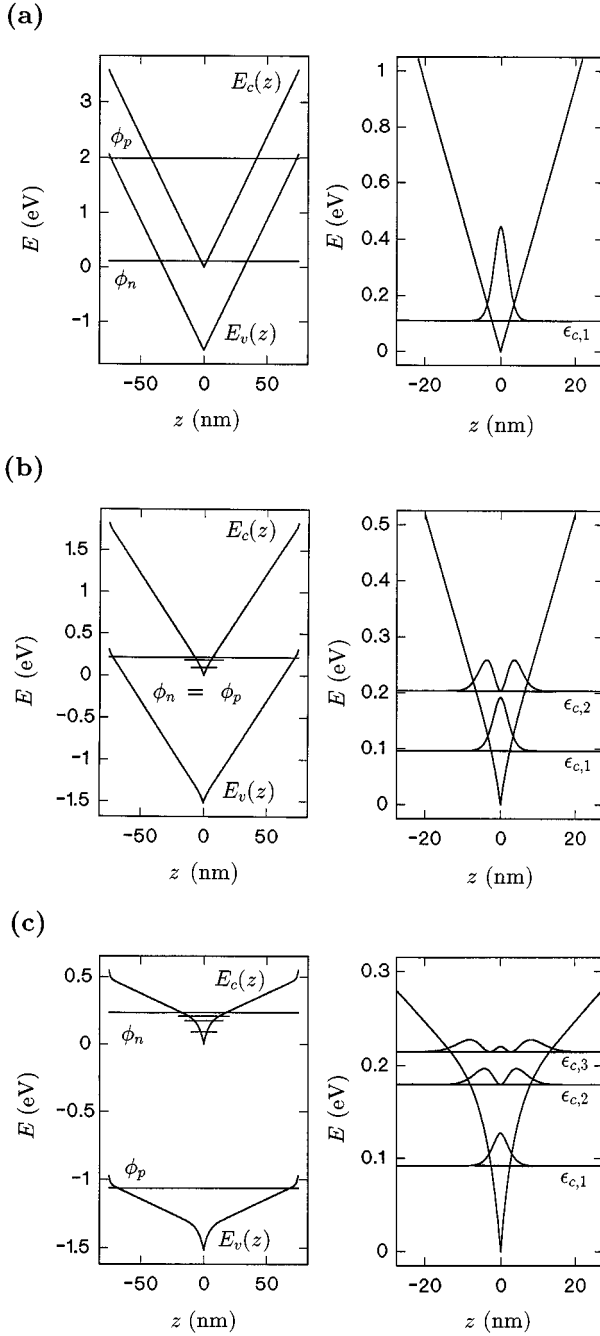
FIG. 5. Self-consistent superlattice potential (left side) and sub-band edges of occupied electronic subbands with squared envelope wave functions (right side) for various excitation levels ($T=0$ K): (a) Almost completely depleted ($\Delta\phi_{np}=-1.88$ V), (b) ground state ($\Delta\phi_{np}=0$ V), and (c) strongly excited ($\Delta\phi_{np}=1.29$ V).

For $n^{(2)}>5.1\times10^{12}$ cm^{-2} three subbands are occupied. Additional $3\rightarrow3$ intrasubband as well as $1\rightarrow3$ and $3\rightarrow1$ intersubband scattering occurs. Note the discontinuous decrease of $\mu_n(n^{(2)})$ due to the instantaneous onset of intersubband scattering.

2. Screening in quasi-2D random-phase approximation

An improved screening theory is the quasi-2D random-phase approximation (quasi-2D RPA) (see, e.g., Ref. 23). It has been applied in several recent studies of transport in
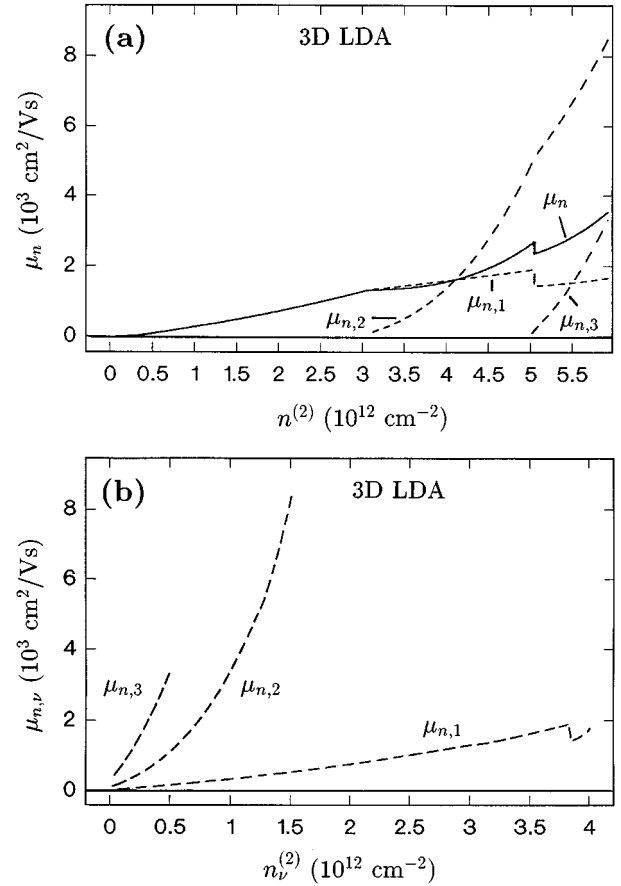
FIG. 6. (a): Calculated subband mobilities (dashed) and the total mobility (solid) as functions of the total electron density. (b): Subband mobilities (dashed) as function of the subband electron densities ($T=0$ K).

δ-doped semiconductors.[25–27] We restrict ourselves to the case of one or two occupied subbands. The scattering matrix element is given by

$$\langle|\langle\psi_{c,\nu,\mathbf{k}_\parallel}|H_{\text{int}}|\psi_{c,\nu',\mathbf{k}_\parallel'=\mathbf{k}_\parallel+\mathbf{q}_\parallel}\rangle|^2\rangle_{\text{average}}=\frac{n_D^{(2)}}{S}(V_{\nu\nu'}^{\text{tot}}(\mathbf{q}_\parallel))^2.\tag{24}$$

$V_{\nu\nu'}^{\text{tot}}(\mathbf{q}_\parallel)$ is the 2D Fourier transform of the scattering matrix element for the screened Coulomb potential averaged in the growth direction over the considered electron wave functions. For its evaluation we need the 2D Fourier transform of the scattering matrix element for the bare Coulomb potential,

$$V_{\nu\nu'}^{\text{ext}}(\mathbf{q}_\parallel)=\frac{2\pi c_0}{q_\parallel}F_{\nu\nu'}^{e,\text{imp}}(\mathbf{q}_\parallel),\tag{25}$$

with the electron-impurity form factor

$$F_{\nu\nu'}^{e,\text{imp}}(\mathbf{q}_\parallel)=\int\varphi_{c,\nu}(z)\varphi_{c,\nu'}(z)\exp(-q_\parallel|z|)dz.\tag{26}$$

$V_{\nu\nu'}^{\text{tot}}(\mathbf{q}_\parallel)$ is given by

$$\sum_{\mu\mu'}\epsilon_{\nu\nu',\mu\mu'}(\mathbf{q}_\parallel)V_{\mu\mu'}^{\text{tot}}(\mathbf{q}_\parallel)=V_{\nu\nu'}^{\text{ext}}(\mathbf{q}_\parallel),\tag{27}$$
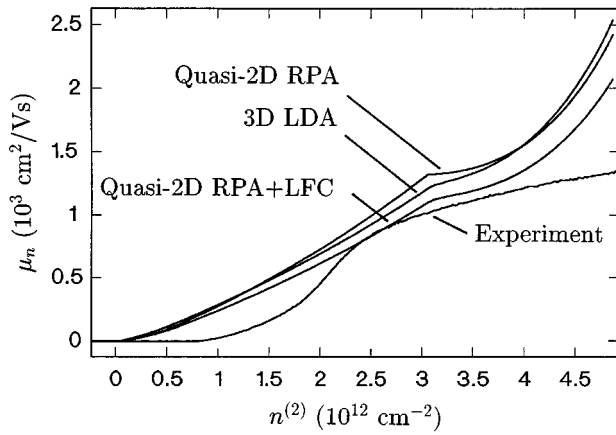
FIG. 7. Comparison of the measured electron-density dependence of the mobility ($T = 4$ K) with the solution of the Boltzmann equation for 3D LDA, quasi-2D RPA, and quasi-2D RPA+LFC screening ($T = 0$ K).

with the static dielectric tensor

$$\epsilon_{\nu\nu',\mu\mu'}(\mathbf{q}_\parallel) = \delta_{\nu\mu}\delta_{\nu'\mu'} + \frac{e^2}{2\epsilon\epsilon_0 q_\parallel}\Pi_{\mu\mu'}(\mathbf{q}_\parallel)F^{e,e}_{\nu\nu',\mu\mu'}(\mathbf{q}_\parallel). \quad (28)$$

$\Pi_{\mu\mu'}(\mathbf{q}_\parallel)$ is the ordinary static polarisation part,[23] and

$$F^{e,e}_{\nu\nu',\mu\mu'}(\mathbf{q}_\parallel) = \int \varphi_{c,\nu}(z)\varphi_{c,\nu'}(z)\varphi_{c,\mu}(z')\varphi_{c,\mu'}(z')$$
$$\times \exp(-q_\parallel|z-z'|)dz\, dz' \quad (29)$$

the electron-electron form factor.

The quasi-2D RPA summarized above and used in Refs. 25–27 is a mean-field theory which neglects both exchange and Coulomb-correlation effects. We consider these short range correlations as local-field corrections within the quasi-2D RPA (quasi-2D RPA+LFC). In the Hubbard approximation[28,29] the dielectric tensor arises from Eq. (28) by multiplying the polarization part $\Pi_{\mu\mu'}(\mathbf{q}_\parallel)$ by $(1 - q_\parallel/2(k^2_{F,\mu} + q^2_\parallel)^{1/2})$.

3. Comparison of experiment and theory

Figure 7 shows a comparison of the measured electron-density dependence of the mobility ($T = 4$ K) with the solution of the Boltzmann equation using 3D LDA, quasi-2D RPA, and quasi-2D RPA+LFC screening for the impurity potentials ($T = 0$ K).

The quasi-2D RPA mobility is almost indistinguishable from the 3D LDA result, which demonstrates that Thomas-Fermi screening is a reasonable approximation for heavily doped δ-n-i-p-i superlattices. The quasi-2D RPA+LFC mobility is smaller than the quasi-2D RPA result because exchange and correlation effects reduce the screening efficiency (increase the scattering probability) of the quasi-2D electron gas.

In the intermediate electron-density regime of 2.5×10^{12} cm^{-2} < $n^{(2)}$ < 4.0×10^{12} cm^{-2}, the quasi-2D RPA+LFC mobility agrees well with the experimental mobility, in particular if one keeps in mind that our calculation started from first principles, containing no fitting parameter but only the

design parameters $n^{(2)}_D$, $n^{(2)}_A$, and d of the investigated sample. The deviation at higher electron density may be due to the fact that the δ-doped donor layers have a small but finite width, whereas we assumed a disappearing layer width for our calculations. The spreading of the donors in the z direction increases the scattering efficiency and reduces the mobility especially for the electrons of the second subband, which have a wave-function node at the center of the doping layer. Thus it seems reasonable that the experimental mobility is slightly smaller than the calculations predicted. The agreement between theory and experiment is also poor at lower electron density. This finding will be analyzed in terms of a disorder-induced MIT in Sec. III C.

C. Metal-insulator transition

The fluctuating disorder potential due to the random distribution of the ionized impurities is responsible for a disorder-induced MIT. This phase transition can be interpreted in a semiclassical or a quantum-mechanical picture—either as percolation transition of the electron fluid in the landscape of the disorder potential or in terms of quantum-mechanical localization of electron wave functions due to disorder.

In the present section, we use the quantum-mechanical approach and apply the self-consistent current-relaxation theory[30] to calculate the mobility in the vicinity of the disorder-induced MIT. In advance we will estimate the density range in which the Boltzmann transport theory is valid. It is sufficient to consider the case of a single occupied subband as the strong experimental deviations from the Boltzmann result occur in this density regime.

1. Ioffe-Regel rule

The Boltzmann transport theory is inadequate to describe the disorder-induced MIT because it assumes plane waves for electrons traveling parallel to the layers, completely neglecting electron localization. Its application is only justified if the mean free path $l_f = v_{F,1}\tau_{c,1}$ of the electrons exceeds their Fermi wavelength $\lambda = 2\pi/k_{F,1}$ (Ioffe and Regel[31]) and the typical impurity separation

$$l_f > \max(\lambda, n^{(2)^{-1/2}}_D). \quad (30)$$

Here $v_{F,1} = \hbar k_{F,1}/m_c$ is the Fermi velocity. Figure 8 shows that this condition is violated for $n^{(2)} < 2.2 \times 10^{12}$ cm^{-2}. The results of the Boltzmann equation are only valid for higher electron density, i.e., exactly for the density regime with good agreement between the quasi-2D RPA+LFC and the experimental mobility in Fig. 7.

2. Self-consistent current-relaxation theory

Gold and Götze introduced a quantum-mechanical mode-coupling theory for the description of the disorder-induced MIT.[30] It is based on a self-consistent treatment of current relaxation and density propagation. Using the continuity equation they derived a system of equations connecting the density propagator
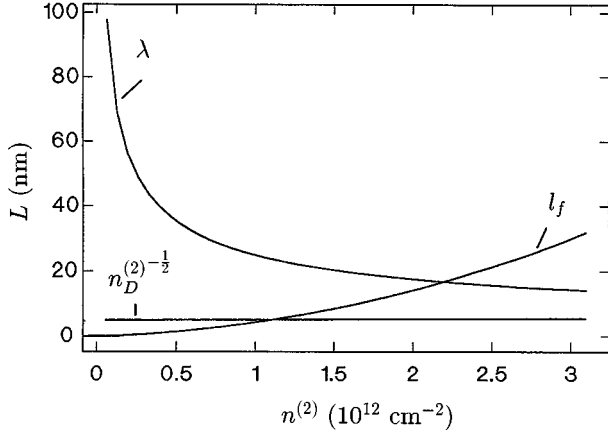
FIG. 8. Electron mean free path, de Broglie wavelength, and typical impurity separation depending on the electron density ($T=0$ K).

$$\Phi(\mathbf{q}_\parallel,\mathcal{Z}) = \frac{\Phi_0(\mathbf{q}_\parallel,\mathcal{Z}+M(\mathcal{Z}))}{1+M(\mathcal{Z})\Phi_0(\mathbf{q}_\parallel,\mathcal{Z}+M(\mathcal{Z}))(\epsilon_{11,11}(\mathbf{q}_\parallel)/\Pi_{11}(\mathbf{q}_\parallel))} \tag{31}$$

of the electron gas in the random disorder potential with its current relaxation kernel

$$M(\mathcal{Z}) = \frac{n_D^{(2)}}{8\pi^2 m_c n^{(2)}} \int d\mathbf{q}_\parallel \, q_\parallel^2 (V_{11}^{\text{ext}}(\mathbf{q}_\parallel))^2 \Phi(\mathbf{q}_\parallel,\mathcal{Z}). \tag{32}$$

$\mathcal{Z}$ denotes the complex frequency.

$$\Phi_0(\mathbf{q}_\parallel,\mathcal{Z}) = \frac{1}{\mathcal{Z}}\left(\frac{\Pi_{11}(\mathbf{q}_\parallel,\mathcal{Z})}{\epsilon_{11,11}(\mathbf{q}_\parallel,\mathcal{Z})} - \frac{\Pi_{11}(\mathbf{q}_\parallel)}{\epsilon_{11,11}(\mathbf{q}_\parallel)}\right) \tag{33}$$

is the density propagator of the free-electron gas. The dynamic dielectric tensor $\epsilon_{11,11}(\mathbf{q}_\parallel,\mathcal{Z})$ is given by Eq. (28) if the static polarisation part $\Pi_{11}(\mathbf{q}_\parallel)$ is replaced by the corresponding dynamic term[30] $\Pi_{11}(\mathbf{q}_\parallel,\mathcal{Z})$ multiplied by $(1-q_\parallel/2(k_{F,1}^2+q_\parallel^2)^{1/2})$ to include local-field corrections. After self-consistently solving Eqs. (31) and (32), the electron mobility in the static limit is obtained from

$$\mu_n = \frac{e}{m_c}\frac{1}{M''(\omega=0)}, \tag{34}$$

where $M''(\omega=0)$ is the imaginary part of the current relaxation kernel.

3. Comparison of theory and experiment

The results of the Boltzmann equation and the selfconsistent current-relaxation theory (SCCRT) for quasi-2D RPA +LFC screening are compared in Fig. 9 with the experimental electron mobility. In contrast to the Boltzmann equation, the SCCRT reproduces the disorder-induced MIT. The calculated critical electron density $n_{\text{MIT}}^{(2)}=1.2\times10^{12}$ cm^{-2} of the MIT (by definition at $T=0$ K) exceeds the experimentally observed value of 1.0×10^{12} cm^{-2} only slightly. This deviation may be in part due to the finite experimental temperature $T=4$ K.
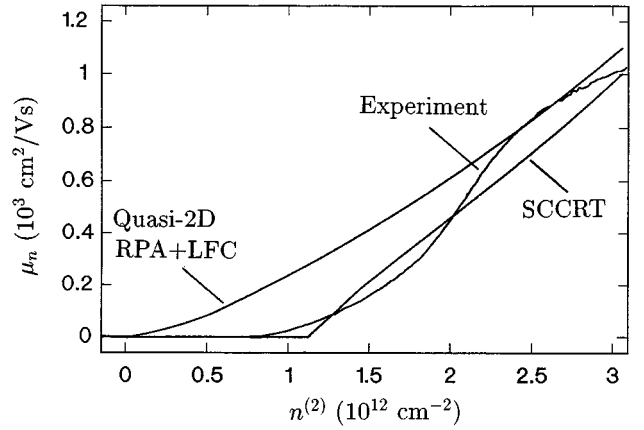
FIG. 9. Comparison of the measured electron-density dependence of the mobility ($T=4$ K) with the results of the Boltzmann equation and the self-consistent current-relaxation theory (SC-CRT) for quasi-2D RPA+LFC screening ($T=0$ K).

IV. POSITIVE MAGNETOCONDUCTIVITY

We focus now on the magnetoconductivity of δ-doped n-i-p-i superlattices in low magnetic fields oriented perpendicular to the doping layers. Detailed studies of gated n-type δ-doped GaAs samples have been reported by Asche et al.[32] All formulas in this section apply to the case of one occupied subband.

According to the scaling theory of localization, 2D metallic systems are weakly localized (for reviews see Refs. 33–35), i.e., the electron states of infinite-size systems are localized even for arbitrary weak disorder. Coherent backscattering reduces the conductivity of finite size 2D metallic systems with length L and electron mean free path l_f in comparison with the classical result of the Boltzmann transport theory at $T=0$ K by

$$\Delta\sigma_n(L) = -\frac{e^2}{\pi^2\hbar}\ln\left(\frac{L}{l_f}\right). \tag{35}$$

The application of a magnetic field B introduces the magnetic length $L_B=\sqrt{\hbar/eB}$ as cutoff for quantum-interference effects. Hence, L has to be replaced by L_B in Eq. (35), which yields a positive logarithmic magnetoconductivity for 2D metallic systems,

$$\Delta\sigma_n(B) = \frac{e^2}{2\pi^2\hbar}\ln\left(\frac{B}{B_0}\right). \tag{36}$$

Electron-electron interaction effects can be introduced in Eq. (36) by multiplication with a prefactor $C_B\lesssim1$.

Figure 10 shows the measured conductivity as a function of the logarithm of the magnetic field for various electron densities ($T=4$ K). In the metallic density regime the observed magnetoconductivity is both positive and proportional to the logarithm of the magnetic field for 0.05 T$<B<0.5$ T. This provides strong evidence of weak localization of the 2D electron gas in our δ-n-i-p-i superlattice. The slope corresponds to $C_B\approx0.6$, which is compatible with theory. For electron densities close to the MIT, the positive magnetoconductivity is strongly reduced, which we attribute to the increasing strength of the disorder potential.
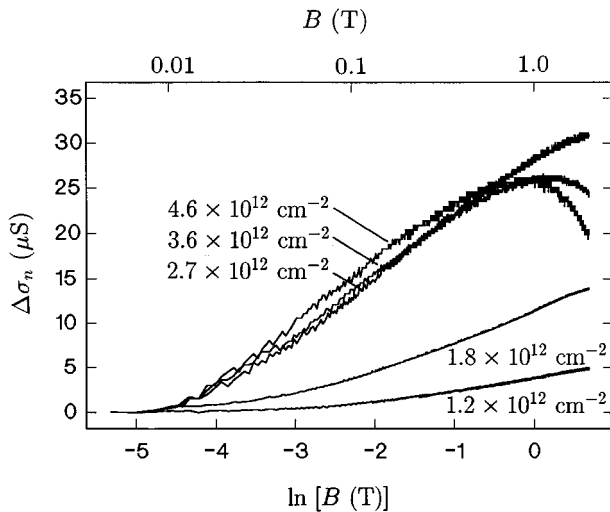
FIG. 10. Experimental positive logarithmic magnetoconductivity ($T=4$ K) for $n^{(2)}=1.2$, 1.8, 2.7, 3.6, and 4.6×10^{12} cm^{-2}, corresponding to zero-field conductivities $\sigma_n=1.4\times10^1$, 8.9×10^1, 3.9×10^2, 6.6×10^2, and 9.6×10^2 μS.

V. TEMPERATURE DEPENDENCE OF THE CONDUCTIVITY

This section is devoted to a detailed discussion of the temperature dependence of the electron conductivity σ_n. Figure 11 shows σ_n as a function of inverse temperature for various electron densities. For $n^{(2)}>2.0\times10^{12}$ cm^{-2} the conductivity shows almost no temperature dependence, i.e., the transport in the heavily doped n layers is of metallic nature with temperature-independent ionized impurity scattering as conductivity-limiting process. Phonon scattering appears to be negligible. On the insulating side of the disorder-induced MIT for $n^{(2)}\leq1.0\times10^{12}$ cm^{-2} activated transport with temperature-independent activation energy is observed at $T\gtrsim100$ K. At lower temperature, however, the activation energy decreases.
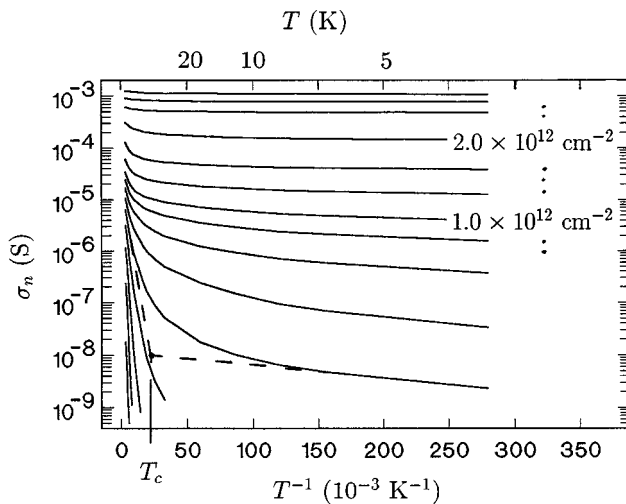
FIG. 11. Temperature dependence of the electron conductivity for various electron densities ($n^{(2)}=0.2,0.3,0.4,0.5,0.6,0.7,0.8,$ 0.9,1.0,1.2,1.5,2.0,3.0,4.0, and 5.0×10^{12} cm^{-2}). T_c defines the transition temperature between activated and hopping transport.
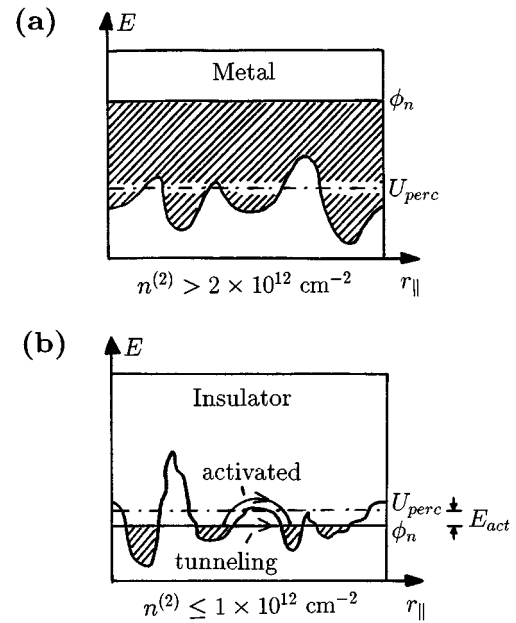
FIG. 12. Influence of the random potential fluctuations on the transport properties of the metallic (a) and insulating regimes (b).

These experimental observations can be explained by introducing a simple semiclassical percolation model:[36,37] The random distribution of the ionized impurities in the doping layers leads to large potential fluctuations which modulate the band edges parallel to the layers. For high electron densities the electronic quasi-Fermi level ϕ_n lies far above the spatially fluctuating band edge [''electron sea with no islands''; Fig. 12(a)]. The electrons travel more or less uniformly through the system only affected by scattering from the fluctuating potential; the transport is *metallic*. If the electron density is gradually reduced the Fermi level decreases and islands with zero (local) electron density appear above the Fermi level. It should be pointed out that the potential fluctuations increase with decreasing electron density due to the less and less efficient screening. The percolation threshold U_{perc} is defined as the energy which marks the Fermi-level position at which the (infinite) electron sea transforms into (finite) ''electron lakes.'' For $\phi_n<U_{\mathrm{perc}}$, electrons have to pass potential barriers in order to get from one lake to another [Fig. 12(b)]. This, however, is impossible at $T=0$ K; the system is *insulating*. Nevertheless, at $T>0$ K electron transport is still possible for $\phi_n<U_{\mathrm{perc}}$ due to the following two processes. Electrons may either perform thermally activated transitions *over* critical potential barriers or hopping (phonon-assisted tunneling) transitions *through* these barriers, the latter requiring less activation energy. The former mechanism, which is dominating at high temperatures, results in an electron-density dependent but temperature independent activation energy $E_{\mathrm{act}}=U_{\mathrm{perc}}-\phi_n$. For lower temperatures hopping transport dominates as the phonon-assisted tunneling probability exceeds the probability for pure activation.

In the following we give a comprehensive analysis of the temperature dependence of the conductivity, starting with the metallic phase. All formulas apply to the case of one occupied subband.
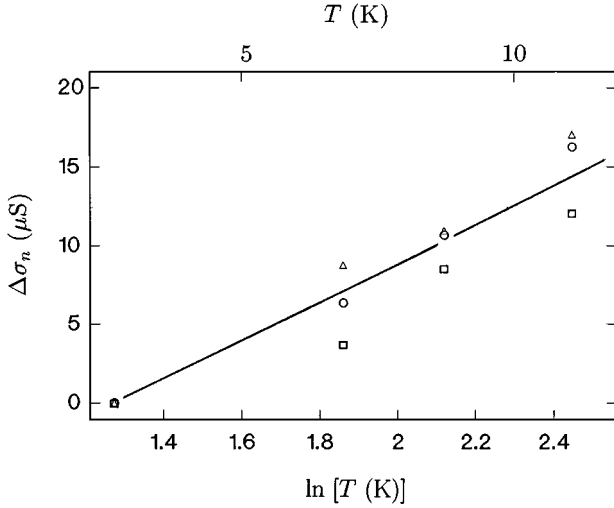
FIG. 13. Low-temperature conductivity in the metallic regime for $n^{(2)} = 2.0$ ($\bigcirc$), 3.0 ($\square$), and 4.0×10^{12} cm^{-2} ($\triangle$), corresponding to zero-field conductivities $\sigma_n = 1.5 \times 10^2$, 4.8×10^2, and 8.7×10^2 μS. The solid line was calculated according to Eq. (37).

A. Metallic phase−weak localization

At finite temperature $T > 0$ K the phase coherence of electron wave functions is destroyed by inelastic scattering processes with a phase-relaxation time τ_φ. For $\tau_\varphi \gg \tau_{c,1}$ the electrons diffuse over a mean distance $L_T = (D\tau_\varphi)^{1/2}$ between two dephasing inelastic processes (experiencing only elastic electron-impurity scattering processes), with D being the diffusion constant. At sufficiently low temperatures where electron-electron scattering is the relevant dephasing process, the temperature dependence $L_T \propto T^{-1/2}$ holds; cf. Ref. 34. L_T acts as a cutoff for quantum-interference phenomena and replaces L in Eq. (35), yielding

$$\Delta\sigma_n(T) = \frac{e^2}{2\pi^2\hbar} \ln\left(\frac{T}{T_0}\right). \tag{37}$$

Electron-electron interaction effects can be included in Eq. (37) by multiplication with a prefactor $C_T \sim 1$; see, e.g., Ref. 33.

A rough estimate for the phase-relaxation time at $T = 4$ K may be obtained from the the magnetic-field dependence depicted in Fig. 10. Deviations from the logarithmic behavior in the metallic density regime occur at $B \approx 0.05$ T as the thermal cutoff length becomes smaller than the magnetic length. From $L_B \approx L_T$ we deduce $L_T \approx 100$ nm, which corresponds to a phase-relaxation time

$$\tau_\varphi = L_T^2/D \approx 1 \times 10^{-12} \text{ s} \gg 5 \times 10^{-14} \text{ s} \approx \tau_{c,1}, \tag{38}$$

(estimating the diffusion constant according to $D = \frac{1}{2} v_{F,1}^2 \tau_{c,1}$).

Figure 13 shows the temperature dependence of the conductivity for three different electron densities in the metallic regime in comparison with the result of Eq. (37). The experimental data comply with the assumption that the conductivity increases due to suppression of weak localization by dephasing electron-electron-scattering processes.
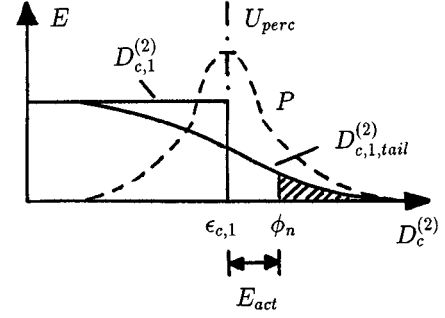
FIG. 14. Sketch of the semiclassical Kane model for band tails.

B. Insulating phase−activated transport

1. Activated transport

The conductivity in the thermally activated regime obeys

$$\sigma_n = \sigma_{0,\text{act}} \exp(-E_\text{act}/k_B T), \tag{39}$$

with prefactor $\sigma_{0,\text{act}}$ and activation energy E_act. Figure 15(a) shows the temperature dependence of σ_n in the high-temperature and low-density regime. It clearly follows Eq. (39), with both $\sigma_{0,\text{act}}$ and E_act being electron density dependent. From the limit $T \to \infty$, we deduce that the prefactor
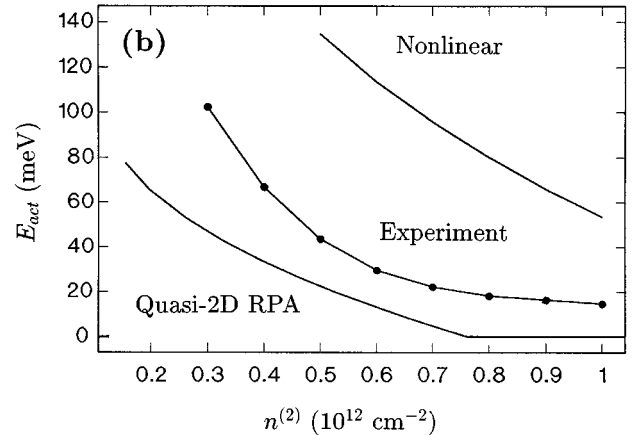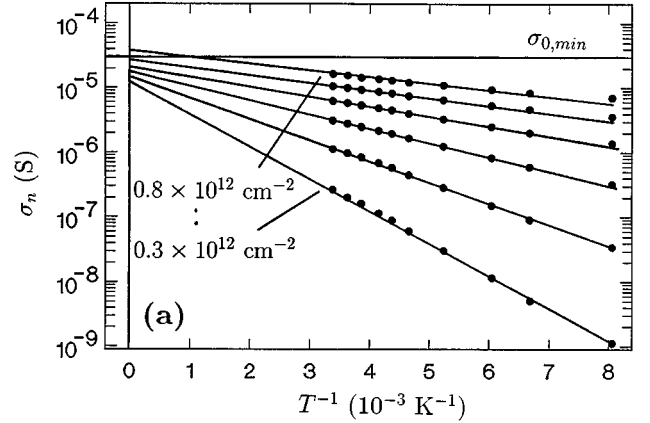
FIG. 15. (a) Activated transport for various electron densities in the insulating phase ($n^{(2)} = 0.3$, 0.4, 0.5, 0.6, 0.7, and 0.8×10^{12} cm^{-2}). The horizontal line corresponds to Mott's minimum metallic conductivity. (b) Dependence of the activation energy on the electron density.

$\sigma_{0,\text{act}}$ grows with increasing electron density. Although Mott's concept[38] of a minimum metallic conductivity $\sigma_{0,\text{min}}$ was disproved by the scaling theory of localization (see, e.g., Ref. 33) it is interesting to note, that our sample's prefactor has the same order of magnitude as $\sigma_{0,\text{min}} \approx 3.0 \times 10^{-5}$ S.[39] A qualitatively similar behavior has been reported by several groups for MOS samples.[5]

For a quantitative description of the electron-density dependence of the activation energy, we use the semiclassical percolation model. First we have to evaluate the distribution function $P(U)$ of the potential fluctuations (Appendix D). We assume a Gaussian distribution

$$P(U) = \frac{1}{\sqrt{2\pi}Q}\exp(-U^2/2Q^2). \qquad (40)$$

Using the linear quasi-2D RPA for screening the width Q is obtained from Eq. (D3) by applying the Parseval formula calculating $V_{11}^{\text{tot}}(\mathbf{q}_\parallel)$ according to Eq. (27) as

$$Q = \left((n_D^{(2)}/(2\pi)^2) \int d\mathbf{q}_\parallel (V_{11}^{\text{tot}}(\mathbf{q}_\parallel))^2 \right)^{1/2}. \qquad (41)$$

Q grows with decreasing electron density because the screening efficiency is reduced. Equation (41) holds in the metallic regime in which the linear-screening approximation is valid. In the insulating regime, however, this expression is inaccurate because the typical fluctuation width exceeds the Fermi energy. Hence we develop a simple, yet reasonable nonlinear model similar to an approach followed in Ref. 1 for 3D heavily doped, heavily compensated bulk material. We start again with Eq. (D3), valid for randomly distributed impurities. In real semiconductor materials, however, the impurities are never completely random distributed as the lattice constant of the host material defines a minimum distance a between neighboring impurities. The width of the potential fluctuations in a circle of radius r large enough to contain many impurities is therefore estimated by

$$Q(r) = \left(n_D^{(2)} \int_a^r 2\pi r' dr' (V(r'))^2 \right)^{1/2}$$
$$= c_0(2\pi n_D^{(2)})^{1/2} \ln(r/a)^{1/2} \qquad (42)$$

if unscreened Coulomb impurity potentials $V(r) = c_0/r$ are used. The resulting expression diverges with increasing radius. The minimum impurity separation $a > 0$ avoids an additional short-range divergence, while the long-range divergence is overcome by screening. In order to understand the screening mechanism, let us consider the standard deviation

$$\Delta n_D^{(2)}(r) = \frac{(n_D^{(2)}\pi r^2)^{1/2}}{\pi r^2} = \frac{n_D^{(2)1/2}}{\sqrt{\pi}r} \qquad (43)$$

of the donor density in the circle. $\Delta n_D^{(2)}(r)$ vanishes with increasing circle size. Therefore long-range donor-concentration fluctuations will be neutralized, no matter how small the electron density is. The screening cutoff radius r_s of the long-range potential fluctuations can be estimated from $\Delta n_D^{(2)}(r_s) = n^{(2)}$ as

$$r_s = \frac{n_D^{(2)1/2}}{\sqrt{\pi}n^{(2)}}. \qquad (44)$$

Within this nonlinear-screening approximation the resulting width of the potential fluctuations is given by Eq. (42) as

$$Q(r_s) = c_0(2\pi n_D^{(2)})^{1/2} \ln(n_D^{(2)1/2}/\sqrt{\pi}n^{(2)}a)^{1/2}. \qquad (45)$$

Q grows only slightly with decreasing electron density. For our δ-n-i-p-i superlattice the prelogarithmic factor is 72 meV. This enormously large value results from the high donor concentration. Surprisingly, the fluctuations are even stronger than in the linear quasi-2D RPA theory, which we attribute to the simplicity of the nonlinear-screening model.

Random potential fluctuations generate band tails which modify the density of states. Applying the Kane model[40] (Fig. 14), we evaluate the modified DOS as a convolution of the undisturbed DOS $D_{c,1}^{(2)}(\epsilon)$ of the first subband [Eq. (13)] and the distribution function $P(U)$ of the potential fluctuations

$$D_{c,1,\text{tail}}^{(2)}(\epsilon) = \int_{-\infty}^{\epsilon} dU P(U) D_{c,1}^{(2)}(\epsilon-U). \qquad (46)$$

In the insulating phase defined by $U_{\text{perc}} - \phi_n \gg 0$ only electrons above the percolation level U_{perc} contribute to transport. Therefore the conductivity is given by

$$\sigma_n \approx e\mu_0 \int_{U_{\text{perc}}}^{\infty} d\epsilon \, D_{c,1,\text{tail}}^{(2)}(\epsilon) \exp(-(\epsilon-\phi_n)/k_BT)$$
$$\approx e\mu_0 k_B T D_{c,1,\text{tail}}^{(2)}(U_{\text{perc}}) \exp(-(U_{\text{perc}}-\phi_n)/k_BT),$$
$$(47)$$

where μ_0 denotes a mobility prefactor for the conducting electrons. Thus we obtain

$$E_{\text{act}} = U_{\text{perc}} - \phi_n \qquad (48)$$

for the activation energy. The percolation level of our 2D continuum problem is given by $U_{\text{perc}} = 0$ because of the symmetry of the applied Gaussian potential distribution $P(U)$ (cf. Ref. 1). In the limit of $k_BT \ll Q$ the quasi-Fermi level ϕ_n is implicitly determined through

$$n^{(2)}(\phi_n) = \int_{-\infty}^{+\infty} d\epsilon \, D_{c,1,\text{tail}}^{(2)}(\epsilon)\Theta(\phi_n-\epsilon). \qquad (49)$$

Figure 15(b) shows the theoretical activation energy calculated from the simple nonlinear as well as quasi-2D RPA screening as well as the experimental result. The activation energy obtained with the simple nonlinear-screening estimate exceeds the linear-screening result. This represents the fact that, as already mentioned, the fluctuations predicted by the nonlinear model are stronger than those of the quasi-2D RPA theory. The experimental values lie between the theoretical curves. In general, the activation energy is extraordinary large due to the large potential fluctuations. It decreases with increasing electron density because the quasi-Fermi level approaches the percolation level. Within the percolation model the critical electron density of the MIT is defined as the density at which E_{act} vanishes.
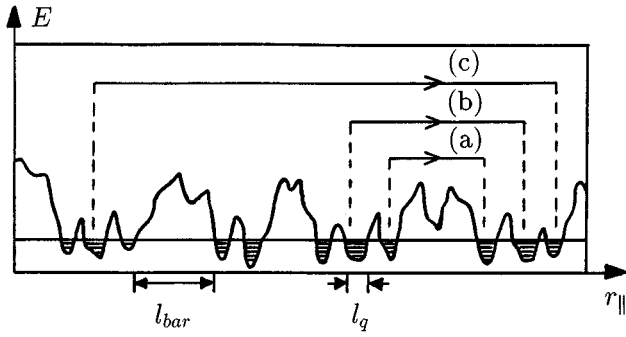
FIG. 16. Band-edge profile of a heavily-doped n-layer with different hopping processes: Nearest-droplet hopping (a), variable-droplet hopping (b), and variable-valley hopping (c).

Quantitative agreement between experiment and percolation model could not be expected due to the following reasons. Instead of performing a self-consistent nonlinear simulation of the potential fluctuations (similar to the semiclassical analysis provided for heterostructure devices by Nixon and Davies[41]), we used simple screening approximations and assumed a symmetric Gaussian distribution function, while the exact distribution function is asymmetric, which implies a nontrivial percolation level (Appendix D). Even more important, the quantization of the electron states parallel to the doping layers in short-range wells of the long-range potential valleys of the fluctuating band edge was neglected completely. A quantitative consideration of these effects is beyond the scope of this paper.

2. Hopping transport

The conductivity in Fig. 11 exhibits a transition from exponentially to weakly temperature-dependent behavior at $T \sim 100$ K. This has been attributed to a transition from thermally activated transport to phonon-assisted tunneling. In order to study the temperature dependence of this hopping transport, we develop a more quantitative model of the potential fluctuations. For our δ-layer case, we proceed in analogy to Ref. 42, where the 3D bulk case has been treated.

Figure 16 shows the band-edge profile of a heavily δ-doped n layer. The potential fluctuates strongly on the length scale

$$l_{\text{bar}} \approx 2r_s \approx \frac{n_D^{(2)1/2}}{n^{(2)}} \qquad (50)$$

due to long-range variations of the impurity concentration [with r_s taken from Eq. (44)]. These fluctuations are accompanied by short-range variations. Thus a small number of potential wells is formed in every long-range potential valley. Because of their low density all electrons condensate in these wells to droplets. In order to determine the temperature dependence of the hopping transport, we have to estimate the typical energy separation between the quantized states in the droplets. Prefactors of the order of unity will be neglected in the estimates given below.

The number of electrons in a short-range well is limited by the number of donors, because otherwise the attractive well would become a repulsive hump. The maximum num-

ber of electrons in a well of diameter l is thus given by the standard deviation of the donor number in this area,

$$N_{\text{drop}}^{(2)}(l) \approx \Delta N_D^{(2)}(l) = (n_D^{(2)}l^2)^{1/2}. \qquad (51)$$

A rough estimate of the depth of typical wells is obtained from Eq. (45), neglecting the logarithmic factor

$$Q \approx c_0 n_D^{(2)1/2}. \qquad (52)$$

The number of electrons in a well of size l and depth Q is not only limited by the Coulomb interaction but also by the Pauli principle to

$$N_{\text{drop}}^{(2)}(l) = l^2 \frac{m_c}{\hbar^2} Q = l^2 \frac{m_c}{\hbar^2} c_0 n_D^{(2)1/2}. \qquad (53)$$

Combining Eqs. (51) and (53) for $N_{\text{drop}}^{(2)}(l)$, we find that the typical diameter of filled droplets

$$l_q = \frac{\hbar^2}{c_0 m_c} \approx 10 \text{ nm} \ll l_{\text{bar}} = \frac{n_D^{(2)1/2}}{n^{(2)}} \qquad (54)$$

is identical with the Bohr radius, but much shorter than the size of the long-range potential valleys.[43] Hence several electron droplets exist in each long-range potential valley. The level spacing of the quantized energy states in such a droplet is approximated through division of its depth by its electron number

$$\Delta \epsilon = \frac{Q}{N_{\text{drop}}^{(2)}(l_q)} = \frac{c_0^2 m_c}{\hbar^2} \approx 10 \text{ meV} \ll E_{\text{act}}. \qquad (55)$$

The numerical values for droplet size and level separation were calculated for GaAs. We want to point out that these values are independent of both the donor and the electron density within our model. On the basis of this investigation of the potential fluctuations, we now analyze the temperature dependence of the hopping transport.

At not too low temperatures hopping processes at the Fermi level between neighboring potential valleys dominate [Fig. 16, case (a)]. Due to their exponential distance dependence, the critical hops which limit the conductivity occur between the nearest electron droplets. The required phonon energy is of the order of $\Delta \epsilon$. This "nearest-droplet" hopping dominates for $k_B T \approx \Delta \epsilon$ corresponding to $T \sim 100$ K, and leads to

$$\sigma_n \approx \sigma_{0,\text{hop}} \exp(-\sqrt{m_c E_{\text{act}}}(l_{\text{bar}}/\hbar) - \Delta \epsilon/k_B T), \qquad (56)$$

with activation energy $\Delta \epsilon \ll E_{\text{act}}$. The first term in the exponent accounts for the involved tunneling process in the WKB approximation.

For $k_B T < \Delta \epsilon$ it is more favorable to minimize the hopping energy at cost of an increased hopping length. The critical hops occur still between neighboring potential valleys but not necessarily between electron droplets of minimum distance [Fig. 16, case (b)]. The hopping length is now approximately $l_{\text{bar}} + \delta l$. Therefore, $\Delta N_D^{(2)}(\delta l) = (n_D^{(2)} \delta l^2)^{1/2}$ energy states of all the electron droplets in the area δl^2 are within reach. Hence one finds for the level spacing of the energy states of all available droplets,

$$\Delta \epsilon(\delta l) = \frac{Q}{\Delta N_D^{(2)}(\delta l)} = \frac{Q}{(n_D^{(2)}\delta l^2)^{1/2}}. \quad (57)$$

The conductivity is given by

$$\sigma_n \approx \sigma_{0,\text{hop}}\exp(-\sqrt{m_c E_{\text{act}}}(l_{\text{bar}}/\hbar)$$
$$-(\sqrt{m_c Q}(\delta l/\hbar) + \Delta\epsilon(\delta l)/k_B T)). \quad (58)$$

The two last competing terms >in the exponent reflect the additional tunneling process in the WKB approximation and the remaining activation energy. The conductivity grows for small δl due to the shorter tunneling path and for large δl due to the smaller activation energy. The optimum additional hopping length is obtained by maximization of σ_n with respect to δl as

$$\delta l_{\text{opt}} = \left(\frac{c_0 \hbar}{\sqrt{m_c Q}k_B T}\right)^{1/2}. \quad (59)$$

Using $\delta l = \delta l_{\text{opt}}$ in Eq. (58), we obtain an expression similar to Mott's law,[44]

$$\sigma_n = \sigma_{0,\text{hop}}\exp(-(T_0/T)^p), \quad (60)$$

with

$$T_0 \approx \frac{c_0}{(\hbar/\sqrt{m_c Q})k_B}, \quad p = \tfrac{1}{2}, \quad (61)$$

the "variable-droplet" hopping law for heavily doped 2D systems. Its range of validity is determined by $l_q < \delta l_{\text{opt}} < l_{\text{bar}}$. For our sample, close to the MIT at $n^{(2)} = 1.0 \times 10^{12}$ cm^{-2}, we estimate "variable-droplet" hopping to dominate for 10 K $< T <$ 80 K.

At still lower temperature critical hops occur between distant potential valleys. The hopping distance is far longer than l_{bar}, and the discrete energy states in the large number of accessible droplets can be replaced by a continuum [Fig. 16, case (c)]. This "variable-valley" hopping obeys Eq. (60) with

$$T_0 \approx \frac{1}{D_c^{(2)}(\phi_n)(\hbar/\sqrt{m_c Q})^2 k_B}, \quad p = \tfrac{1}{3} \quad (62)$$

if the DOS $D_c^{(2)}(\phi_n)$ at the quasi-Fermi level is energy independent (derivation in analogy to Ref. 45, using $\hbar/\sqrt{m_c Q}$ as localization radius of the droplet electrons). If the DOS exhibits a linear Coulomb gap at the quasi-Fermi level ($D_c^{(2)}(\phi_n \pm \epsilon) \approx \epsilon/c_0^2$), Eq. (60) again holds, but with Eq. (61) being exactly reproduced instead of Eq. (62) (the derivation runs in analogy to Ref. 46).

Thus a continuous transition occurs in the hopping regime with decreasing temperature from "nearest-droplet" hopping to "variable-droplet" hopping, and finally to full "variable-valley" hopping. The temperature dependence alters from activated behavior to Mott's law. The characteristic exponent changes gradually from $p = \tfrac{1}{2}$ to $p = \tfrac{1}{3}$ if the DOS at the Fermi level is constant. If a Coulomb gap exists, $p = \tfrac{1}{2}$ applies for both "variable-droplet" and "variable-valley" hopping.
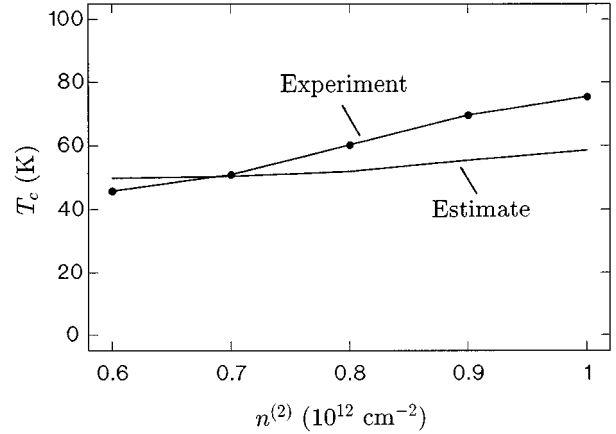
FIG. 17. Dependence of the transition temperature between activated and hopping transport on the electron density.

At present, a quantitative comparison with experiment is impossible because not enough data are available for the hopping regime. Instead we study the transition region between thermally activated transport and "nearest-droplet" hopping.

3. Transition between activated and hopping transport

Using linear fits for both the activated and hopping regimes, we define an experimental transition temperature T_c (see Fig. 11). At the transition temperature, the thermally activated conductivity [Eq. (39)] and the "nearest-droplet" hopping conductivity [Eq. (56)] are identical by definition. Neglecting preexponential factors, we obtain

$$-E_{\text{act}}/k_B T_c \approx -\sqrt{m_c E_{\text{act}}}(l_{\text{bar}}/\hbar) - \Delta\epsilon/k_B T_c, \quad (63)$$

from which we evaluate

$$T_c = \frac{\sqrt{E_{\text{act}}}\hbar}{\sqrt{m_c}l_{\text{bar}}k_B} = \frac{\sqrt{E_{\text{act}}}\hbar}{\sqrt{m_c}k_B}\frac{n^{(2)}}{n_D^{(2)1/2}}. \quad (64)$$

in combination with Eqs. (50) and (55). Figure 17 shows that the result of Eq. (64) (using the measured activation energy) and the experimentally observed transition temperature are in reasonable agreement. The high values of 40 K $\leq T_c \leq$ 80 K reflect the large magnitude of the potential fluctuations in the heavily δ-doped n layers.

VI. SUMMARY

In conclusion, we performed a comprehensive experimental and theoretical study of the transport properties of heavily δ-doped n-i-p-i superlattices in dependence of magnetic field and temperature in the range of 4–300 K. Our results demonstrate that such structures represent a unique quasi-2D model system for the investigation of the disorder-induced metal-insulator transition.

The electron density in the donor layers doped to 6.6×10^{12} cm^{-2} was varied between 0 and 5.5×10^{12} cm^{-2} by applying a bias voltage between the selectively contacted n- and p-type layers. Special emphasis was put on the electron-density dependence of the low-temperature mobility recorded at 4 K. In the truly metallic regime, mobilities of

about 1000 cm^2/V s were measured in agreement with the multisubband Boltzmann transport theory. Near the metal-insulator transition observed at an electron density of 1.0×10^{12} cm^{-2}, we calculated the mobility with the self-consistent current-relaxation theory, which even gives an accurate estimate for the electron density at the transition. Concerning the impurity-scattering efficiency and, hence, the screening of ionized donors in δ-doped electron layers, we found that the 3D local-density approximation works surprisingly well compared with the quasi-2D random-phase approximation. Evidence of weak localization is provided by the observation of both positive logarithmic magnetic-field and temperature dependences of the conductivity in the metallic regime. In the insulating phase, at temperatures above 100 K, we observed activated transport with a huge density-dependent activation energy of up to 100 meV, in reasonable agreement with a model based on semiclassical percolation. At lower temperature the activation energy decreases, which we attribute to phonon-assisted tunneling through the barriers of the disorder potential. In this hopping regime, we studied the temperature-dependence of the conductivity based on the detailed properties of the fluctuating potential in δ-doped layers. The predicted transition temperature between activated and hopping transport is in agreement with experiment.

ACKNOWLEDGMENTS

APPENDIX A

In order to determine the actual doping concentrations, the p-layer conductance versus bias-voltage characteristics $G_{pp}(U_{np})$ was measured at $T = 300$ K and subsequently analyzed. From this result we deduced U_{np}^{th} and $G_{pp}(0 \text{ V})$ $/G_{pp}(U_{np}^{\text{th}})$ which was transformed into the corresponding conductance quotient $G_{pp}^{nipi}(0 \text{ V})/G_{pp}^{nipi}(U_{np}^{\text{th}})$ of the n-i-p-i region [eliminating the contact resistances in analogy to Eq. (C4)]. Remember that only the n layers are depleted at U_{np}^{th}, whereas the p-layer conductivity remains finite.

Then we postulated that the actual doping concentrations are found if the result of a Thomas-Fermi calculation (Sec. II) fulfills both

$$U_{np,\text{TF}}^{\text{th}} \approx U_{np}^{\text{th}} \tag{A1}$$

and

$$p^{(2)}(0V)/p^{(2)}(U_{np,\text{TF}}^{\text{th}}) \approx G_{pp}^{nipi}(0V)/G_{pp}^{nipi}(U_{np}^{\text{th}}). \tag{A2}$$

The second condition implies that the hole mobility $\mu_p(U_{np})$ is constant in the interval $U_{np}^{\text{th}} \leqslant U_{np} \leqslant 0$ V at

$T = 300$ K. In order to verify this assumption, we measure dG_{pp}^{nipi}/dU_{np} as well as $dp^{(2)}/dU_{np}$ by capacitance-voltage profiling to evaluate $dG_{pp}^{nipi}(U_{np})/dp^{(2)}(U_{np}) \propto \mu_p(U_{np})$. The hole mobility turned out to be almost independent of U_{np} at room temperature in the considered range. This result is not surprising as the hole density is even at the threshold with $p^{(2)} = n_A^{(2)} - n_D^{(2)} = 1.1 \times 10^{12}$ cm^{-2} still quite high.

Thus we have two linear independent conditions (A1) and (A2) for the determination of two doping concentrations $n_A^{(2)}$ and $n_D^{(2)}$. To find the corresponding values we performed a numerical fit in the two-dimensional parameter space spanned by the impurity densities, taking advantage of both the high accuracy and high speed of the Thomas-Fermi method.

APPENDIX B

The consideration of band tails within the Thomas-Fermi method (Sec. II) imposes no fundamental problems. Applying the Kane model,[40] we replace the DOS in the density equation (3) for $n^{(3)}(z)$ by the corresponding DOS including band tails $D_{c,\text{tail}}^{(3)}(\epsilon, z)$ which is obtained as a convolution of the distribution function of the potential fluctuations $P(U, z)$ with the original DOS $D_c^{(3)}(\epsilon, z)$ given by Eq. (5),

$$D_{c,\text{tail}}^{(3)}(\epsilon, z) = \int_{-\infty}^{\epsilon} dU P(U, z) D_c^{(3)}(\epsilon - U, z). \tag{B1}$$

The numerical effort is, however, considerably increased as the calculation involves an additional self-consistence loop: The electron-density profile $n^{(3)}(z)$ depends on $P(U, z)$, which in turn depends on the screening properties of the electron gas, i.e., on $n^{(3)}(z)$.

How to calculate $P(U, z)$ is not obvious because a closed expression for the screening of the impurity potentials valid for both the nonlinear insulating and the linear metallic screening regime is not available. We use the semiclassical 3D LDA screening, i.e., a Yukawa-shaped donor potential [Eq. (21)], and apply an approximation with exponential band tails[47] for $P(U, z)$. The fluctuation width is calculated according to Eq. (D3).

APPENDIX C

The evaluation of the electron mobility $\mu_n(n^{(2)})$ and conductivity $\sigma_n(n^{(2)})$ requires knowledge of the geometric sample dimensions and the contact resistances. Figure 18 shows a typical n layer of our δ-n-i-p-i sample. The total layer resistance along the current path consists of the resistance $R_{b,n}^{nipi}(n^{(2)}(U_{np}), \mu_n(n^{(2)}))$ of the n-i-p-i bar region, the resistances $R_{c,n}^{nipi}(n^{(2)}(U_{np}), \mu_n(n^{(2)}))$ of the two n-i-p-i contact regions, the resistances $R_{c,n}^{nini}$ of the two n-i-n-i regions, and the two contact resistances $R_{c,n}$. The measured resistance is thus given by

$$\frac{1}{G_{nn}(U_{np})} = \frac{1}{N_{\text{per}}}(R_{b,n}^{nipi}(n^{(2)}, \mu_n) + 2R_{c,n}^{nipi}(n^{(2)}, \mu_n)$$

$$+ 2R_{c,n}^{nini} + 2R_{c,n})$$
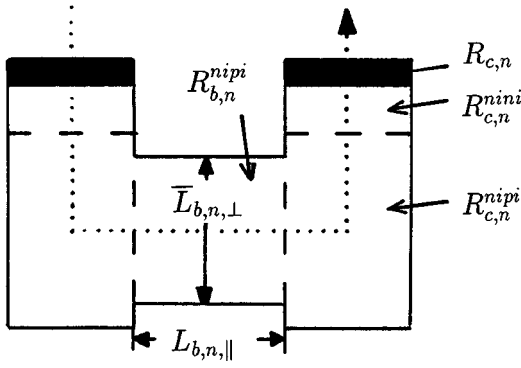
FIG. 18. Resistance regions of a n-layer of the δ-n-i-p-i device. The dotted line marks the current path.

$$= \frac{1}{en^{(2)}\mu_n} \frac{L_{b,n,\parallel}}{N_{\text{per}}\bar{L}_{b,n,\perp}} + \frac{1}{en^{(2)}\mu_n} K_n^{\text{contact}}$$
$$+ R_n^{\text{contact}}. \tag{C1}$$

$L_{b,n,\parallel}$ and $\bar{L}_{b,n,\perp}$ are the length and average width of the bar, and N_{per} the number of n layers. These three parameters are known while the unspecifiable current path in the n-i-p-i contact region is hidden in the constant K_n^{contact} and the n-i-n-i as well as contact resistances in R_n^{contact}. Both constants were determined from Eq. (C1) using a linear fit after the measurement of $G_{nn}(U_{np})$ for several samples with different bar length $L_{b,n,\parallel}$.

According to Eq. (C1) the transformation formulas from the measured bias-voltage-dependent conductance into the electron-density dependent conductivity and mobility run

$$\sigma_n(n^{(2)}) = \left(\frac{L_{b,n,\parallel}}{N_{per}\bar{L}_{b,n,\perp}} + K_n^{\text{contact}} \right) G_{nn}^{nipi}(U_{np}) \tag{C2}$$

and

$$\mu_n(n^{(2)}) = \left(\frac{L_{b,n,\parallel}}{N_{\text{per}}\bar{L}_{b,n,\perp}} + K_n^{\text{contact}} \right) \frac{G_{nn}^{nipi}(U_{np})}{en^{(2)}(U_{np})}, \tag{C3}$$

respectively. $n^{(2)}(U_{np})$ was calculated with the improved Thomas-Fermi method (Sec. II, Appendix B). Here

$$G_{nn}^{nipi}(U_{np}) = \frac{1}{\left(\dfrac{1}{G_{nn}(U_{np})} - R_n^{\text{contact}} \right)} \tag{C4}$$

denotes the conductance of the n-i-p-i region obtained from the measured $G_{nn}(U_{np})$ data by eliminating the contact resistances.

APPENDIX D

The basis for the calculation of the distribution function of the potential fluctuations is the linear superposition principle for the ionized impurity potentials. This assumption is justified both for bare unscreened Coulomb potentials and the linear-screening regime at high electron density if the quasi-Fermi level is far exceeding the width of the potential fluctuations. Our results do not apply to the nonlinear-screening regime for low electron density. For a review on the 3D bulk case, see Ref. 48.

If we consider one n layer, neglecting all remote doping layers, the distribution function due to $N_D^{(2)}$ positive donors j with electrostatic potential $V(\mathbf{r}_{\parallel,j})$ in a sheet of area S is obtained from the following ensemble average over all possible impurity configurations

$$P(U) = \left\langle \delta\left(U - \sum_{j=1}^{N_D^{(2)}} V(\mathbf{r}_{\parallel,j}) \right) \right\rangle,$$

$$\langle \cdots \rangle = S^{-N_D^{(2)}} \prod_{j=1}^{N_D^{(2)}} \int_S \cdots d\mathbf{r}_{\parallel,j}. \tag{D1}$$

A couple of rather tedious transformations finally yields in the limit $S \to \infty$ for fixed impurity density $n_D^{(2)}$

$$P(U) = \frac{1}{\pi} \int_0^\infty ds\, \exp\left(n_D^{(2)} \int [\cos(sV(\mathbf{r}_\parallel)) - 1]d\mathbf{r}_\parallel \right)$$
$$\times \cos\left(sU - n_D^{(2)} \int \sin(sV(\mathbf{r}_\parallel))d\mathbf{r}_\parallel \right). \tag{D2}$$

The second moment of the generally asymmetric distribution function $P(U)$, i.e., the width of the potential fluctuations, is given by

$$Q = \left(n_D^{(2)} \int d\mathbf{r}_\parallel (V(\mathbf{r}_\parallel))^2 \right)^{1/2}. \tag{D3}$$

The extension of these results from one n-layer to δ-n-i-p-i superlattices with a large but finite number of n and p layers is cumbersome but straightforward. However, for the δ-n-i-p-i sample considered in this work, the influence of remote doping layers is negligible due to the large interlayer distance compared to the screening length of the p-layer hole gases. The result of Eq. (D2) is approximated either by a Gaussian distribution or a distribution with exponential band tails proposed by Unger.[47] Both are exact up to the second moment, having in particular the correct fluctuation width.

[1] B. I. Shklovskii and A. L. Efros, *Electronic Properties of Doped Semiconductors*, Springer Series in Solid-State Sciences Vol. 45 (Springer, Berlin, 1984).

[2] *Electron-Electron Interactions in Disordered Systems*, edited by A. L. Efros and M. Pollak (North-Holland, Amsterdam, 1985).

[3] *Disordered Semiconductors*, edited by M. A. Kastner, G. A. Thomas, and S. R. Ovshinsky (Plenum, New York, 1987).

[4] H. Stupp *et al.*, Phys. Rev. Lett. **71**, 2634 (1993); A. Gaymann, H. P. Geserich, and H. v. Löhneysen, *ibid.* **71**, 3681 (1993); T. F. Rosenbaum, G. A. Thomas, and M. A. Paalanen, *ibid.* **72**, 2121 (1994); H. Stupp *et al.*, *ibid.* **72**, 2122 (1994); P. Dai, Y. Zhang, and M. P. Sarachik, Phys. Rev. B **49**, 14 039 (1994); S. Bogdanovich, P. Dai, M. P. Sarachik, and V. Dobrosavljevic, Phys. Rev. Lett. **74**, 2543 (1995).

[5] T. Ando, A. B. Fowler, and F. Stern, Rev. Mod. Phys. **54**, 437 (1982).

[6] J. L. Robert *et al.*, Phys. Rev. B **33**, 5983 (1986).

[7] Y. J. Wang, B. D. McCombe, and W. Schaff, Surf. Sci. **263**, 547 (1992).

[8] A. Zrenner *et al.*, Semicond. Sci. Technol. **3**, 1132 (1988).

[9] G. Tempel, F. Koch, H. P. Zeindl, and I. Eisele, J. Phys. (Paris) **48** Suppl. C5, 259 (1987).

[10] See, e.g., S. Koch, R. J. Haug, K. v. Klitzing, and K. Ploog, Phys. Rev. Lett. **67**, 883 (1991); H. W. Jiang, C. E. Johnson, K. L. Wang, and S. T. Hannahs, *ibid.* **71**, 1439 (1993); T. Wang *et al.*, *ibid.* **72**, 709 (1994); A. A. Shashkin *et al.*, *ibid.* **73**, 3141 (1994).

[11] A. Zrenner, Ph.D. thesis, Technische Universität München, 1987.

[12] R. Dötzer *et al.*, Semicond. Sci. Technol. **9**, 1332 (1994).

[13] G. H. Döhler, Phys. Status Solidi B **52**, 79 (1972); **52**, 533 (1972).

[14] G. H. Döhler, Surf. Sci. **73**, 97 (1978); J. Vac. Sci. Technol. **16**, 851 (1979).

[15] G. H. Döhler, G. Hasnain, and J. N. Miller, Appl. Phys. Lett. **49**, 704 (1986).

[16] K. H. Gulden *et al.*, Appl. Phys. Lett. **62**, 3180 (1993).

[17] K. Schrüfer *et al.*, J. Appl. Phys. **72**, 4992 (1992).

[18] P. Ruden and G. H. Döhler, Phys. Rev. B **27**, 3538 (1983).

[19] J. C. Slater, Phys. Rev. **81**, 385 (1951).

[20] A. Zrenner and F. Koch, Surf. Sci. **196**, 671 (1988); E. Skuras *et al.*, Semicond. Sci. Technol. **6**, 535 (1991); Th. Ihn, K.-J. Friedland, R. Hey, and F. Koch, Phys. Rev. B **52**, 2789 (1995); A. B. Henriques, L. C. D. Gonçalves, P. L. de Souza, and B. Yavich, Semicond. Sci. Technol. **11**, 190 (1996).

[21] E. D. Siggia and P.C. Kwok, Phys. Rev. B **2**, 1024 (1970).

[22] S. Mori and T. Ando, Phys. Rev. B **19**, 6433 (1979).

[23] G. Bastard, *Wave Mechanics Applied to Semiconductor Heterostructures* (Halsted, New York, 1988).

[24] N.W. Ashcroft and N.D. Mermin, *Solid State Physics* (Holt, Rinehart and Winston, New York, 1976).

[25] L. R. González, J. Krupski, and T. Szwacka, Phys. Rev. B **49**, 11 111 (1994).

[26] G.-Q. Hai, N. Studart, and F. M. Peeters, Phys. Rev. B **52**, 8363 (1995).

[27] A. B. Henriques, Phys. Rev. B **53**, 16 365 (1996).

[28] J. Hubbard, Proc. R. Soc. London Ser. A **243**, 336 (1957).

[29] M. Jonson, J. Phys. C **9**, 3055 (1976).

[30] A. Gold and W. Götze, Phys. Rev. B **33**, 2495 (1986).

[31] A. F. Ioffe and A.R. Regel, Prog. Semicond. **4**, 237 (1960).

[32] M. Asche *et al.*, Superlatt. Microstruct. **10**, 425 (1991); Semicond. Sci. Technol. **7**, 923 (1992).

[33] P. A. Lee and T. V. Ramakrishnan, Rev. Mod. Phys. **57**, 287 (1985).

[34] B. L. Altshuler and A. G. Aronov, in *Electron-Electron Interactions in Disordered Systems* (Ref. 2), p. 1.

[35] H. Fukuyama, in *Electron-Electron Interactions in Disordered Systems* (Ref. 2), p. 155.

[36] J. M. Ziman, J. Phys. C **1**, 1532 (1968).

[37] E. Arnold, Surf. Sci. **58**, 60 (1976).

[38] N. F. Mott, Philos. Mag. **26**, 1015 (1972).

[39] D. C. Licciardello and D.J. Thouless, J. Phys. C **8**, 4157 (1975).

[40] E. O. Kane, Phys. Rev. **131**, 79 (1963).

[41] J. A. Nixon and J. H. Davies, Phys. Rev. B **41**, 7929 (1990).

[42] B. I. Shklovskii, Fiz. Tekh. Poluprovodn. **7**, 112 (1973) [Sov. Phys. Semicond. **7**, 77 (1973)].

[43] Strictly speaking, Eqs. (51) and (53) yield as l_q not the typical but the maximum droplet size. In order to see that l_q is also the minimum droplet size we have to consider the exact expression (42) instead of Eq.(52) for the fluctuation amplitude. $Q(r \approx l)$ decreases with decreasing droplet size l. Therefore a droplet of size l_q does not split into smaller droplets because these together would not have enough quantum states to accommodate the electrons of the parental droplet.

[44] N. F. Mott, J. Non-Cryst. Solids **1**, 1 (1968).

[45] W. Brenig, G. H. Döhler, and H. Heyszenau, Philos. Mag. **27**, 1093 (1973).

[46] A. L. Efros and B. I. Shklovskii, J. Phys. C **8**, L49 (1975).

[47] K. Unger, in *Semiconductor Optoelectronics*, edited by M. A. Herman (Polish Scientific, Warszawa, 1980), p. 13.

[48] P. Van Mieghem, Rev. Mod. Phys. **64**, 755 (1992).